nature

https://doi.org/10.1038/s41586-020-2081-7

Supplementary information

In situ NMR metrology reveals reaction mechanisms in redox flow batteries

In the format provided by the authors and unedited

Evan Wenbo Zhao, Tao Liu, Erlendur Jónsson, Jeongjae Lee, Israel Temprano, Rajesh B. Jethwa, Anqi Wang, Holly Smith, Javier Carretero-González, Qilei Song & Clare P. Grey✉

Supplementary Information

In Situ NMR Metrology Reveals Reaction Mechanisms in Redox Flow Batteries

Evan Wenbo Zhao,[1] Tao Liu,[1,5] Erlendur Jónsson,[1,2] Jeongjae Lee,[1,6] Israel Temprano,[1] Rajesh B. Jethwa,[1] Anqi Wang,[3] Holly Smith,[1] Javier Carretero-González,[4] Qilei Song,[3] Clare P. Grey[1]*

Affiliations:

[1]Department of Chemistry, University of Cambridge, Cambridge, UK

[2]Department of Physics, Chalmers University of Technology, Gothenburg, Sweden

[3]Barrer Centre, Department of Chemical Engineering, Imperial College London, London, UK

[4]Institute of Polymer Science and Technology, ICTP-CSIC, Madrid, Spain

[5]Present address: Shanghai Key Laboratory of Chemical Assessment and Sustainability, Department of Chemistry, Tongji University, Shanghai, China.

[6]Present address: School of Earth and Environmental Sciences, Seoul National University, Seoul, South Korea

*email: cpg27@cam.ac.uk

Calculations

(i) Electron spin density distribution

DFT calculations of singly occupied molecular orbitals were performed using the Gaussian16 code[53]. The spin-polarized B3LYP functional was used in combination with the 6-31G(d) basis set for structural relaxation and a more extensive EPR-III basis set[54]. Designed for EPR parameter computations, this enabled hyperfine coupling constants to be calculated.

(ii) NMR chemical shifts calculations of the decomposition products dihydroxyanthrone (DHA) and dihydroxyanthrol (DHAL)

Tetramethylsilane (TMS) and DHA, both the keto and enol form (*i.e.* DHA and DHAL, inlay in Extended Data Fig. 8d), were geometry optimised with DFT calculations. The final structures were verified to be minima by inspecting their vibrational frequencies. In each case, NMR chemical shift calculations were performed. The ORCA program package was used[55]. The calculations used the B3LYP DFT functional with the D3 dispersion correction along with the def2-TZVPP basis set[56-58]. The RIJCOSX approximation was used with the appropriate auxiliary basis sets, def2/J and also additionally the AutoAux option for the NMR step[59]. In each case, tight SCF and optimisation criteria were used along with the following grid settings: Grid5, FinalGrid6 and GridX4.

(iii) Calculations of equilibrium concentrations and the comproportionation equilibrium constant

Starting from the equilibrium reactions[13],

$$AQ^{2-} + e^- \rightleftharpoons AQ^{3\bullet-},\ K_1 = \frac{[AQ^{3\bullet-}]}{[AQ^{2-}]} \tag{S1}$$

$$AQ^{3\bullet-} + e^- \rightleftharpoons AQ^{4-},\ K_2 = \frac{[AQ^{4-}]}{[AQ^{3\bullet-}]} \tag{S2}$$

$$AQ^{2-} + AQ^{4-} \rightleftharpoons AQ^{3\bullet-},\ K_c = \frac{[AQ^{3\bullet-}]^2}{[AQ^{2-}][AQ^{4-}]} \tag{S3}$$

Using $K_n = \exp(\frac{ZF}{RT}E_n)$ where Z is the number of electrons (here $Z = 1$), E_n is the redox potential of the n^{th} redox reaction, we note that

$$K_c = \frac{K_1}{K_2} = \exp[\frac{ZF}{RT}(E_1 - E_2)] \tag{S4}$$

Under the assumption that the system is in a state of equilibrium, we can obtain estimates of the relative populations of AQ^{2-}, $AQ^{3\bullet-}$ and AQ^{4-}. Starting from 100% SOC, removing n electrons results in the formation of x $AQ^{3\bullet-}$ and y AQ^{2-}. Therefore, $n = x + 2y$. The SOC can be expressed as $SOC = 1 - \frac{n}{2} = 1 - \frac{x}{2} - y$. The relative concentrations are then $[AQ^{2-}] = y$, $[AQ^{3\bullet-}] = x$, and $[AQ^{4-}] = 1 - x - y$.

Following on and working from the comproportionation equilibrium constant, $K_c = \frac{x^2}{y(1-x-y)}$, rearranging the equation gives:

$$(\frac{K_c}{2}-2)x^2 - K_c x + K_c(n-\frac{1}{2}n^2) = 0 \quad \text{(S5)}$$

Solving for x gives two solutions:

If $K_c \neq 4$,

$$x = \frac{K_c \pm \sqrt{K_c{}^2 - (K_c-4)(2n-n^2)K_c}}{K_c - 4} \quad \text{(S6)}$$

If $K_c = 4$,

$$x = n - \frac{1}{2}n^2 \quad \text{(S7)}$$

Thus, for a given number of electrons, n, and a comproportionation equilibrium constant, K_c, the fraction of $AQ^{3\bullet-}$, the fraction of AQ^{2-}, and the fraction of AQ^{4-}, can be derived to be x, y and $1 - x - y$ respectively.

After recasting this in terms of SOC, these values can be evaluated for DHAQ, where E_1-E_2 is reported to be 60 mV and thus K_c = 10.35 based on modelling of the CV data[13]. This is shown in Extended Data Fig. 4e, along with other K_c values for illustrative purposes. Another way to look at the data is to consider the relative concentrations at 50% SOC as a function of K_c (Extended Data Fig. 4f).

Equations S6 and S7 were also used to fit experimental data (Fig. 2c of main text). A SOC lag parameter was also used as an offset to aid in the fitting, to compensate for the experimental data points above 100% SOC. Likely causes of this skew include the re-oxidation or degradation of $DHAQ^{4-}$. The concentration of $AQ^{3\bullet-}$ along with the skewed SOC is then used to derive K_c. A lag of 8-12% is displayed, along with the fits in Extended Data Fig. 4g. The fitted K_c values are as follows: 3.72, 3.72, 3.71, 3.68 and 3.64. Thus the fitted voltage differences according to Eq. S4 are between 32.6 mV and 33.2 mV, *i.e.*, 33 mV.

To obtain an error estimate for the E_1-E_2 value determined with this method, the radical fraction was also derived using ±½ the FWHM of the peak. This gave a lower bound of 22 mV and upper bound of 44 mV for E_1-E_2. Table S1 gives the full list of values. This analysis was performed so as to compare the accuracy of this approach with the values for E_1-E_2 determined by analysis of the CV measurements.

Supplementary Table 1. The fitted equilibrium constant, K_c, from the experimentally derived radical fractions, Exp. while +½ FWHM and -½ FWHM are radical fractions derived taking ± FWHM of the peak as the experimental value. The lag parameter is an offset in the SOC of the system. The voltage differences, E_1-E_2, are calculated with equation S4.

	K_c			E_1-E_2		
Lag parameter	**Exp.**	**+½ FWHM**	**-½ FWHM**	**Exp.**	**+½ FWHM**	**-½ FWHM**
8%	3.71	5.58	2.47	33.1	43.4	22.8
9%	3.72	5.60	2.46	33.2	43.5	22.7
10%	3.71	5.59	2.45	33.1	43.5	22.6
11%	3.68	5.56	2.43	32.9	43.3	22.4
12%	3.64	5.51	2.39	32.6	43.1	22.0

(iv) Bulk magnetic susceptibility and radical concentrations

For a cylindrical sample tube, the solvent chemical shift is related to the paramagnetic susceptibility by

$$\Delta\delta_s = \frac{4}{3}\pi\Delta\chi \tag{S8}$$

where $\Delta\delta_s$ is the chemical shift in parts per million and $\Delta\chi$ is the magnetic susceptibility.

The molar paramagnetic susceptibility χ_M is defined as

$$\chi_M = \chi V_M \tag{S9}$$

where V_M is the molar volume of the radicals in m^3/mol. Combining Eq. S8 and S9 gives

$$\Delta\delta_s = \frac{4}{3}\pi\frac{\Delta\chi_M}{V_M} \tag{S10}$$

The molar volume V_M is related to the concentration of radicals C_{rad} by

$$V_M = \frac{1}{C_{rad}} \tag{S11}$$

χ_M can be calculated by

$$\chi_M = \frac{N_A\mu^2}{3k_BT} \tag{S12}$$

where N_A is Avogadro's number, k_B is the Boltzmann constant in CGS units, T is the temperature in Kelvin and μ is the magnetic moment of the unpaired electron in CGS units, given by

$$\mu = 2\beta\sqrt{S(S+1)} \tag{S13}$$

where β is the Bohr magneton, S is the total spin quantum number of electron (S = ½ when there is one unpaired electron).

By substituting μ, Eq. S12 becomes

$$\chi_M = \frac{N_A(2\beta)^2 S(S+1)}{3k_B T} \tag{S14}$$

Combining Eq. S10, S11 and S14, then rearranging the equation:

$$C_{rad} = \frac{9k_B T}{16\pi N_A \beta^2 S(S+1)}\Delta\delta_s \tag{S15}$$

Finally, by plugging in the values of the constants,

$$C_{rad} = 183.33\Delta\delta_s \tag{S16}$$

the radical concentration is proportional to the chemical shift change by a factor of 183.33 mol/m^3.

(v) Cyclic voltammetry fitting

Following the logic and equations from Oldham and Myland[60], we have made modifications to reflect the two-electron process. Here, we have written the modified equations for z-electrons. Numbers in parenthesis refer to the equation numbering scheme of the Oldham and Myland paper:

$$\textit{(2:4)}\ \frac{\pm I(t)}{zFAk^{o'}} = C_R^s(t)\exp\left\{\frac{\pm z\alpha F}{RT}\left[E(t)-E^{o'}\right]\right\} - C_P^s(t)\exp\left\{\frac{\mp(1-\alpha)zF}{RT}\left[E(t)-E^{o'}\right]\right\}$$

$$\textit{(4:1)}\ j_R^s(t) = \frac{\mp I(t)}{zFA}\ \text{and (4:2)}\ j_P^s(t) = \frac{\mp I(t)}{zFA}$$

$$\textit{(4:4)}\ \xi(t) = \exp\left\{\frac{\pm zF}{RT}\left[E(t)-E^{o'}\right]\right\}$$

$$\textit{(7:7)}\ I(t) = \frac{\pm zFAC_R^b\dfrac{\sqrt{D_R}}{\sqrt{\delta}}}{1+\dfrac{\sqrt{D_R}}{\xi(t)\sqrt{D_P}}} - \sum_{n=1}^{N-1} w_n I\left(\frac{N-n}{N}\right)t$$

$$\textit{(8:3)}\ I(t) = \frac{\pm zFAC_R^b\dfrac{\sqrt{D_R}}{\sqrt{\delta}} - \left(1+\dfrac{\sqrt{D_R}}{\xi(t)\sqrt{D_P}}\right)\displaystyle\sum_{n=1}^{N-1} w_n I\left(\frac{N-n}{N}\right)t}{1+\dfrac{\sqrt{D_R}}{\xi(t)\sqrt{D_P}}+\dfrac{\sqrt{D_R}}{k^{o'}[\xi(t)]^{\alpha}\sqrt{\delta}}}$$

(vi) Nuclear transverse relaxation in electron-transfer reactions

The system can be treated as a diamagnetic species (anion) in exchange with a radical anion, with concentrations of the diamagnetic and paramagnetic species, [*D*] and [*P*], respectively. For a system in equilibrium, [*D*] and [*P*] are related to the relative lifetimes of the different species. The fractions of paramagnetic and diamagnetic species (f_P and f_D, respectively) are given by,

$$f_P = \frac{[P]}{[P]+[D]} = \frac{\tau_P}{\tau_P + \tau_D} \tag{S17}$$

$$f_D = \frac{[D]}{[P]+[D]} = \frac{\tau_D}{\tau_P + \tau_D} \tag{S18}$$

where τ_P and τ_D are the lifetimes of the paramagnetic and diamagnetic species. The inverse of the lifetimes τ_P^{-1} and τ_D^{-1} are the transition probabilities (or frequencies) for conversion from the paramagnetic to the diamagnetic species and vice versa, respectively.

The bimolecular rate constant k_{ex} for the exchange reaction (shown in Fig. 3a of the main text) is defined as,

$$[N] = k_{ex}[P][D] \tag{S19}$$

Where [*N*] is the number of moles of electrons transferred per litre, per unit time. The transition probabilities (τ_D^{-1} and τ_P^{-1}) are then related to the rate constant via:

$$\tau_D^{-1} = \frac{[N]}{[D]} = k_{ex}[P] \tag{S20}$$

$$\tau_P^{-1} = \frac{[N]}{[P]} = k_{ex}[D] \tag{S21}$$

For example, if k_{ex} is 10^5 $(M.s)^{-1}$, [*P*] is 0.001 M and [*D*] is 0.1 M, the number of electrons transferred per second will be 10 $M.s^{-1}$. At equilibrium, the transition probability from the paramagnetic to the diamagnetic molecule is 10^4 s^{-1} (or Hz), from the diamagnetic to the paramagnetic molecule is 10^2 s^{-1} (or Hz).

This situation is analogous to a two-site chemical exchange process between a paramagnetic and diamagnetic species, which has been treated in detail in Chapter 6 of reference 19, by Bertini *et al.* The observables in the NMR experiments are the proton signals of the two species. At the onset of charge, the diamagnetic species is in a large excess compared to the paramagnetic species, thus simplified expressions can be derived and are given in S22 and S23 (Eqns. 6.17 and 6.18 in reference 19).

In the slow exchange regime, when the transverse relaxation rate of the paramagnetic species, R_{2P}, is much faster than the exchange rate (strictly, the transition probability of the paramagnetic species, τ_P^{-1}), *i.e.*, $R_{2P} \gg \tau_P^{-1}$, the transverse relaxation rate of the diamagnetic species, R_{2ex}, arising from the chemical exchange with the paramagnetic species, is given by[19]:

$$R_{2ex} = f_P \tau_P^{-1} \tag{S22}$$

and is independent of R_{2P}. In the fast exchange regime where $\tau_P^{-1} \gg (\Delta\omega)^2 \tau_P \gg R_{2P}$ (with $\Delta\omega$ being the frequency difference between the paramagnetic and diamagnetic proton NMR signals), R_{2ex} is given by,

$$R_{2ex} = f_P (\Delta\omega)^2 \tau_P \tag{S23}$$

Replacing f_P by $\frac{[P]}{[P]+[D]}$ and τ_P^{-1} by $k_{ex}[D]$ in Eqns. S22 and S23, and when $[D] \gg [P]$, R_{2ex} becomes:

$$R_{2ex} = [P] k_{ex} \text{ (slow exchange)} \tag{S24}$$

$$R_{2ex} = (\Delta\omega)^2 \cdot \frac{[P]}{([D]+[P]) \cdot [D]} \cdot \frac{1}{k_{ex}} \text{ (fast exchange)} \tag{S25}$$

Supplementary Figures

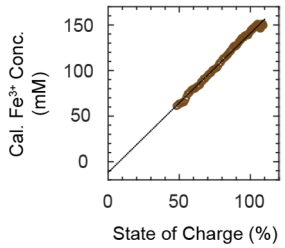

Supplementary Figure 1 | Concentration of ferricyanide (Fe^{3+}) calculated based on the Evans' method as a function of SOC assuming the spin-only value for Fe^{3+}. As charging progresses, ferrocyanide (diamagnetic) is oxidised to ferricyanide (paramagnetic, low spin, $S = ½$). Via the Evans' method, the concentration of ferricyanide can be estimated from the shift of the water resonance from the *operando* NMR spectra (Extended Data Figure 2a). The concentration of ferricyanide increases linearly as a function of SOC, in agreement with the continuous oxidation of Fe^{2+} to Fe^{3+}. The calculated susceptibility is 1.5 times higher than predicted based on the spin-only value for a $S = ½$ ion. CN^- and OH^- exchange, which has been reported in literature, may account for the difference since $Fe(H_2O)_6^{3+}$ is high spin[61]. Deviations from the spin-only value are likely due to incomplete quenching of the orbital angular momentum contribution for this t_{2g}^5 ion[62]. Further investigations are in progress to investigate the magnetism in this system.

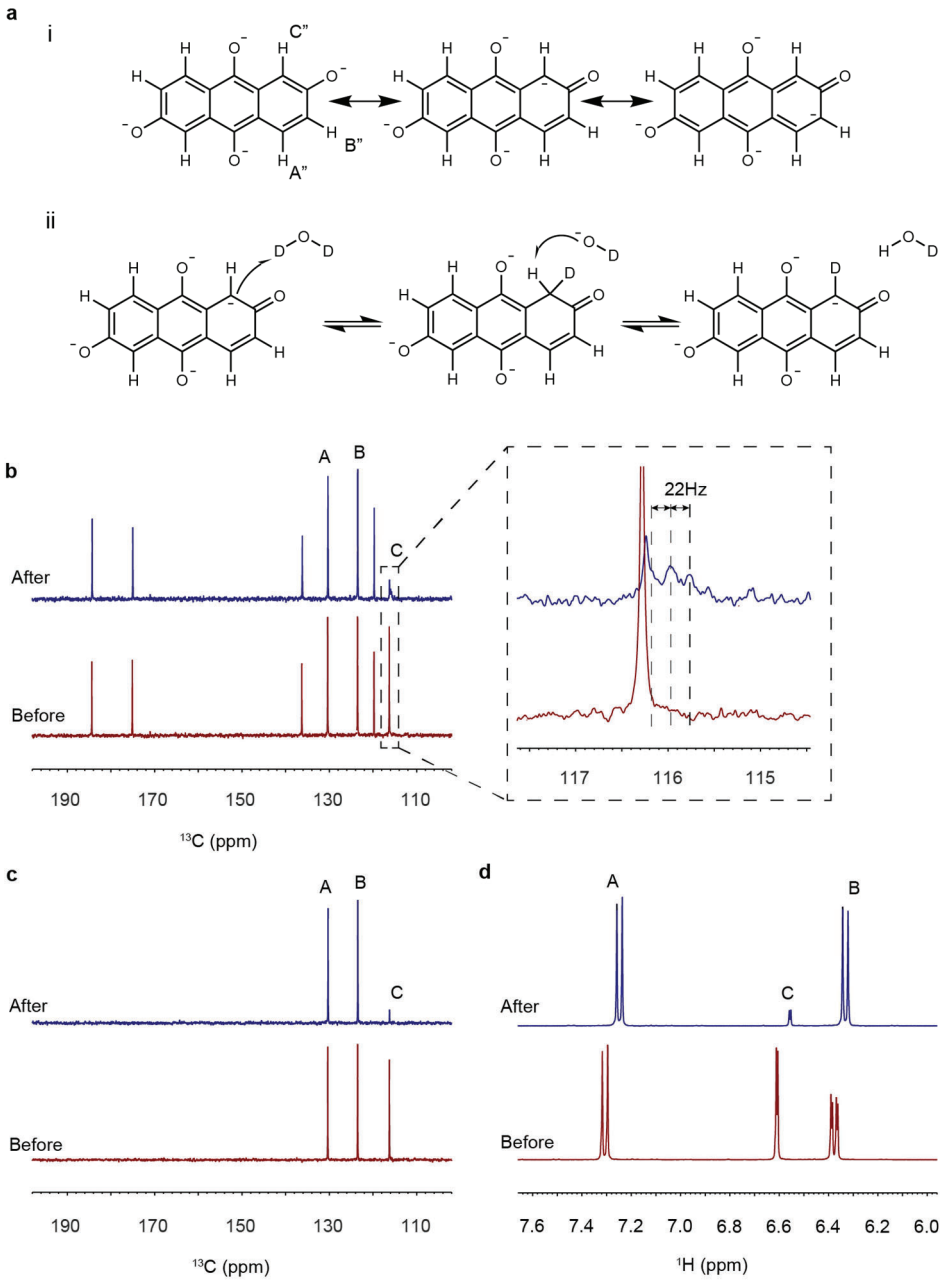

Supplementary Figure 2 | NMR evidence of H-D exchange. a, i) Resonance structures of 2,6-DHAQ^{4-}. The resonance structure shown in the middle retains aromaticity and is therefore preferred to the structure on the right where the aromaticity is lost. ii) Mechanism of the H-D exchange reaction. **b**, *Ex situ* one-pulse ^{13}C and **c**, DEPT ^{13}C NMR spectra of 2,6-DHAQ^{2-} acquired before and after first reduction cycle. C-D triplet coupling pattern in ^{13}C NMR spectrum suggests that an H-D exchange reaction with the solvent D_2O for reduced DHAQ at site C" took place. **d**, *Ex situ* ^{1}H NMR spectra of 2,6-DHAQ^{2-} acquired before and after ten galvanostatic cycles. The intensity decrease of signal C" suggests that the H-D exchange reaction took place. The shift of the peaks could be caused by the slight pH change or a DHAQ concentration change as water crosses over the membrane.

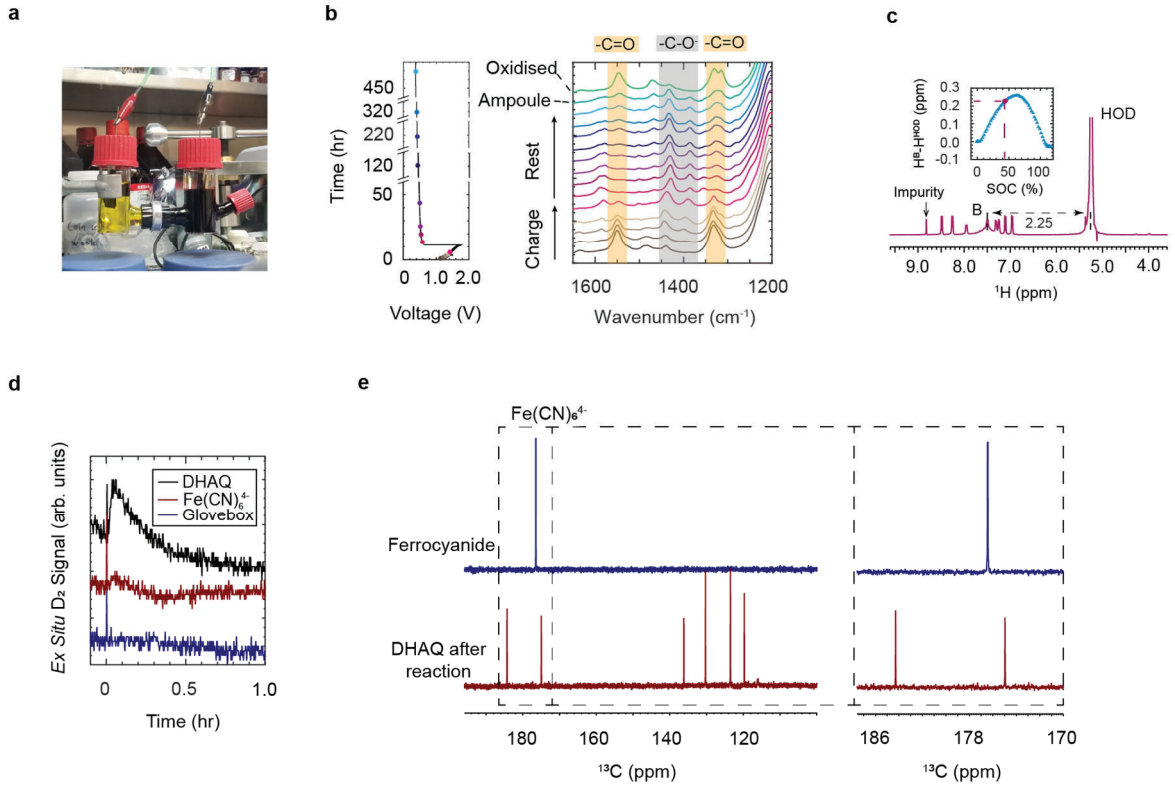

Supplementary Figure 3 | IR, NMR and MS analysis during the H-cell experiment. a, Picture of the *ex situ* H-cell in an Ar glovebox. **b**, H-cell voltage profile and IR spectra acquired at different states of charge in a charge-rest experiment inside the Ar glovebox. The yellow bars highlight the vibrational modes of the -C=O groups; the grey bars highlight the vibrational modes of -C-O$^-$ group. The spectrum of the aliquot taken from the H-cell after charging and stored in an opaque ampoule for 470 hours is labelled "Ampoule" in the figure. The "Oxidised" spectrum refers to a 0.2 cm^3 aliquot taken at 470 hrs which was subsequently oxidised by bubbling 15 cm^3 of air through it using a syringe. The intensity of C=O vibrational modes at 1350 cm^{-1} and 1550 cm^{-1} decrease while the intensity of -C-O$^-$ vibrational modes at 1400 cm^{-1} and 1450 cm^{-1} increase during charging. During cell resting, this trend reverses. This indicates the re-oxidation of DHAQ^{4-} and DHAQ$^{3\bullet-}$. At 470 hr, the relative intensities of the -C-O$^-$ and C=O vibrational modes resemble those at approximately 50% SOC, suggesting that about half of the DHAQ^{4-} was re-oxidised. **c**, *Ex situ* ^{1}H NMR spectrum of the oxidised sample sealed in a gas-tight tube. The inset shows the change of the chemical shift separation between B and HOD as a function of SOC, as measured by *in situ* NMR. The chemical shift separation between B and HOD of the H-cell sample was measured to be 2.25 ppm, corresponding to either 40-50% SOC (as highlighted by the purple dot) or 50-60% SOC, depending on the side of the parabolic curve that is used. **d**, *Ex situ* mass spectrometry signals of D_2 (m/z = 4) of 2 cm^3 gas extracted from the headspace of the catholyte and anolyte compartment of the H-cell and from the Ar glovebox. A signal corresponding to D_2 was detected from the DHAQ electrolyte compartment while a much weaker signal was detected from the $K_4Fe(CN)_6$ side. **e**, ^{13}C NMR spectra of ferrocyanide and the DHAQ aliquot ("Oxidised") from the H-cell after the charge-rest experiment.

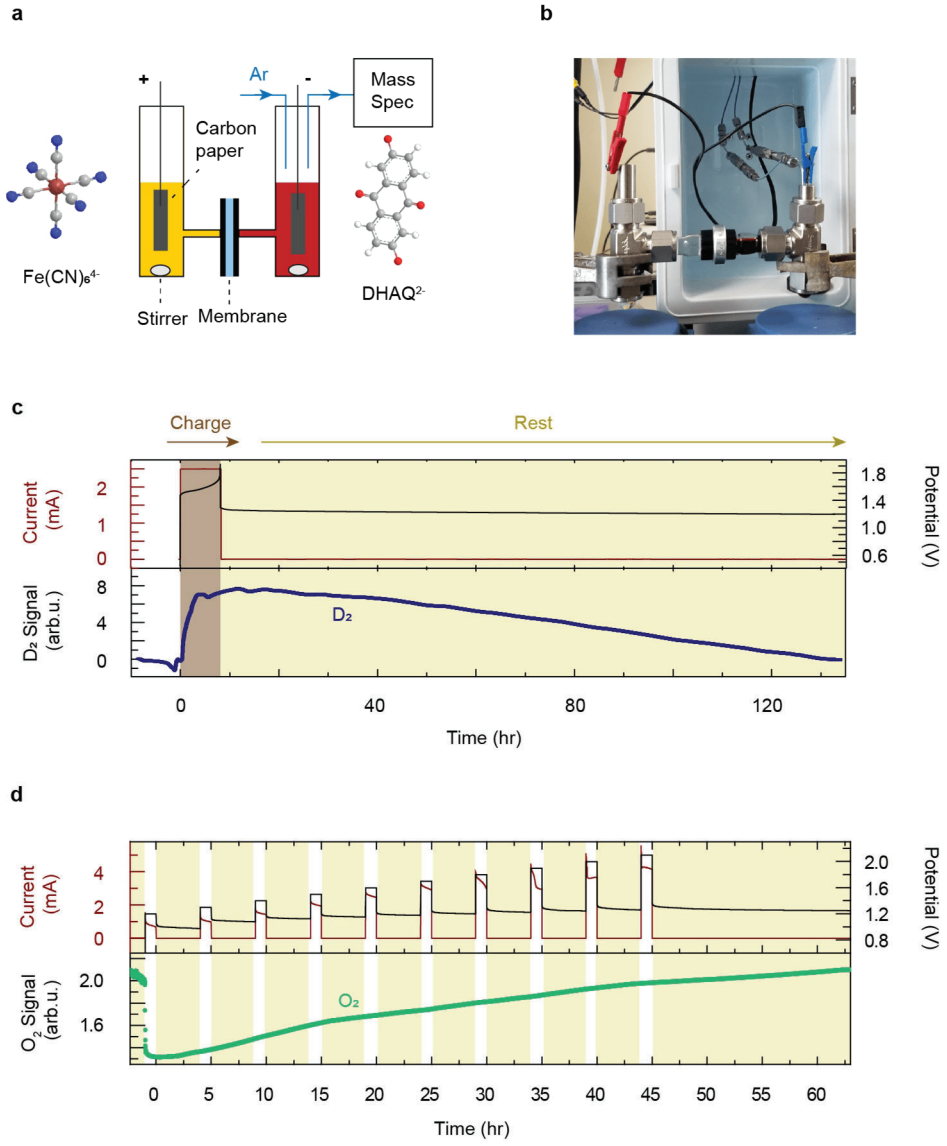

Supplementary Figure 4 | *In situ* MS: detection of D_2 and O_2 signals. a, Schematic and **b**, picture of the H-cell for *in situ* mass spectrometry. **c**, Mass spectrometry signals of D_2 (m/z = 4) during a charge-rest experiment. DHAQ (8.3 cm^3, 60 mM) and $K_4Fe(CN)_6$ (8.3 cm^3, 180 mM) were loaded into the respective separate electrolyte compartments of the H-cell and separated by a Nafion membrane. It shows that D_2 gas evolves as soon as the charge commences (2.5 mA to a cut-off voltage of 1.9 V). Furthermore, gas evolution continues during battery rest, *i.e.* the D_2 generation is a chemical reaction. The D_2 signal slowly decreases as $DHAQ^{4-}$ is re-oxidised over the course of 120 hours. **d**, *In situ* mass spectrometry signals of O_2 (m/z = 32) during a stepwise potential hold-rest experiment. DHAQ (8 cm^3, 100 mM) and $K_4Fe(CN)_6$ (8 cm^3, 300 mM) were loaded into the relevant electrolyte compartment. The drop in O_2 signal intensity upon applying the reductive potential is due to the consumption of the impurity, oxygen, by the reduced $DHAQ^{3\bullet-}$ and $DHAQ^{4-}$, in the gas line of the MS. This follows the anthraquinone process, *i.e.* $DHAQ^{4-} + D_2O + \frac{1}{2}O_2 \rightarrow DHAQ^{2-} + D_2O_2$.

Supplementary Table 2. The charge and SOC for each potential-hold step. The total SOC amounts to 26.68% after all the steps.

Potential (V)	Charge (mAh)	SOC (%)
1.2	0.80	0.83
1.3	1.06	1.10
1.4	1.50	1.56
1.5	2.01	2.09
1.6	2.55	2.65
1.7	3.04	3.16
1.8	3.40	3.53
1.9	3.35	3.48
2.0	3.73	3.87
2.1	4.25	4.41
Total	25.69	26.68

References

53. Gaussian 16 Rev. B.01 (Wallingford, CT, 2016).

54. Barone, V. Recent Advances in Density Functional Methods, Part I, *World Scientific Publ. Co.*, *Singapore*, (1996)

55. Neese, F. The ORCA program system. *WIREs: Comput. Mol. Sci.* **2**, 73-78 (2012).

56. Grimme, S., Ehrlich, S. & Goerigk, L. Effect of the damping function in dispersion corrected density functional theory. *J. Comput. Chem.* **32**, 1456-1465 (2011).

57. Grimme, S., Antony, J., Ehrlich, S. & Krieg, H. A consistent and accurate ab initio parametrization of density functional dispersion correction (DFT-D) for the 94 elements H-Pu. *J. Chem. Phys.* **132**, 154104 (2010).

58. Weigend, F. & Ahlrichs, R. Balanced basis sets of split valence, triple zeta valence and quadruple zeta valence quality for H to Rn: Design and assessment of accuracy. *Phys. Chem. Chem. Phys.* **7**, 3297-3305 (2005).

59. Weigend, F. Accurate Coulomb-fitting basis sets for H to Rn. *Phys. Chem. Chem. Phys.* **8**, 1057-1065 (2006).

60. Oldham, K. B. & Myland, J. C. Modelling cyclic voltammetry without digital simulation. *Electrochim. Acta* **56**, 10612-10625 (2011).

61. J. Luo et al., Unraveling pH dependent cycling stability of ferricyanide/ferrocyanide in redox flow batteries. *Nano Energy* **42**, 215-221 (2017).

62. I. Bertini, C. Luchinat, F. Mani, A. Scozzafava, Adducts of bis(N-substituted ethylenediamine) copper(II) complexes with hexacyanoferrate(III). *Inorg. Chem.* **19**, 1333-1336 (1980).